

Journal Pre-proof

Nickel-iron nanoparticles encapsulated in carbon nanotubes prepared from waste plastics for low-temperature solid oxide fuel cells

Qingyu Liu, Faze Wang, Enyi Hu, Ru Hong, Tao Li, Xiangzhou Yuan, Xin-Bing Cheng, Ning Cai, Rui Xiao, Huiyan Zhang



PII: S2589-0042(22)01127-0

DOI: <https://doi.org/10.1016/j.isci.2022.104855>

Reference: ISCI 104855

To appear in: *ISCIENCE*

Received Date: 10 April 2022

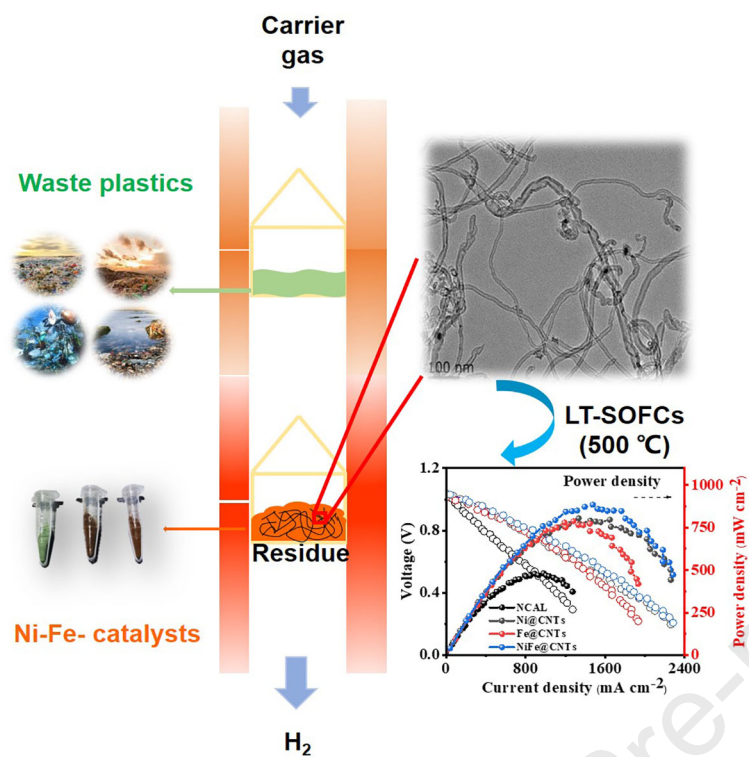
Revised Date: 17 June 2022

Accepted Date: 23 July 2022

Please cite this article as: Liu, Q., Wang, F., Hu, E., Hong, R., Li, T., Yuan, X., Cheng, X.-B., Cai, N., Xiao, R., Zhang, H., Nickel-iron nanoparticles encapsulated in carbon nanotubes prepared from waste plastics for low-temperature solid oxide fuel cells, *ISCIENCE* (2022), doi: <https://doi.org/10.1016/j.isci.2022.104855>.

This is a PDF file of an article that has undergone enhancements after acceptance, such as the addition of a cover page and metadata, and formatting for readability, but it is not yet the definitive version of record. This version will undergo additional copyediting, typesetting and review before it is published in its final form, but we are providing this version to give early visibility of the article. Please note that, during the production process, errors may be discovered which could affect the content, and all legal disclaimers that apply to the journal pertain.

© 2022 The Author(s).



**Nickel-iron nanoparticles encapsulated in carbon nanotubes prepared
from waste plastics for low-temperature solid oxide fuel cells**

Qingyu Liu^a, Faze Wang^a, Enyi Hu^a, Ru Hong^a, Tao Li^a, Xiangzhou Yuan^b, Xin-Bing
Cheng^a, Ning Cai^c, Rui Xiao^a, Huiyan Zhang^{a, d, *}

^a Key Laboratory of Energy Thermal Conversion and Control of Ministry of Education,
School of Energy and Environment, Southeast University, Nanjing 210096, PR China

^b Korea Biochar Research Center, APRU Sustainable Waste Management Program &
Division of Environmental Science and Ecological Engineering, Korea University,
Seoul 02841, Republic of Korea

^c State Key Laboratory of Coal Combustion, School of Energy and Power Engineering,
Huazhong University of Science and Technology, Wuhan 430074, PR China

^d Lead contact

*Corresponding author. E-mail: hyzhang@seu.edu.cn. Tel.: +86-25-83790667.

Summary

Low-temperature solid oxide fuel cells (LT-SOFCs) are a promising next-generation fuel cell due to their low cost and rapid start-up, posing a significant challenge to electrode materials with high electrocatalytic activity. Herein, we reported the bimetallic nanoparticles encapsulated in carbon nanotubes (NiFe@CNTs) prepared by carefully controlling catalytic pyrolysis of waste plastics. Results showed that plenty of multi-walled CNTs with outer diameters (14.38 ± 3.84 nm) were observed due to the smallest crystalline size of Ni-Fe alloy nanoparticles. SOFCs with such NiFe@CNTs blended in anode exhibited remarkable performances, reaching a maximum power density of 885 mW cm^{-2} at 500°C . This could be attributed to the hierarchical architecture well-dispersed alloy nanoparticles and high graphitization degree of NiFe@CNTs to improve HOR activity. Our strategy could upcycle waste plastics to produce nanocomposites and demonstrate a high-performance LT-SOFCs system, addressing the challenges of sustainable waste management and guaranteeing global energy safety simultaneously.

Keywords: Waste plastics; Bimetallic catalysts; Carbon nanotubes; Low-temperature solid oxide fuel cells (LT-SOFCs); Waste-to-energy

Introduction

Solid oxide fuel cells (SOFCs) are as electrochemical energy conversion devices that can continuously produce electricity as long as the fuel inputs are supplied (Zhang et al., 2021b). They have been recognized as one of the most promising technologies for fulfilling increasing energy demands and the worldwide problem of climate change owing to its high efficiency, low emissions, and fuel flexibility. Currently, a significant challenge of traditional SOFC lies in the high operating temperatures ($> 750\text{ }^{\circ}\text{C}$), resulting in performance degradation, technical complexity, economic barriers and limited applications (Mushtaq et al., 2021a). Significant efforts have been made around the world to address the aforementioned issues in order to reduce the operating temperature of SOFCs to the intermediate or low-temperature (LT) region (c.a. $400\text{-}600\text{ }^{\circ}\text{C}$), which ultimately decreases marketing costs and overcome the commercialization barrier (Hu et al., 2021).

The limited performances of LT-SOFCs are attributed to several factors, such as low ionic conductivity ($< 0.1\text{ S cm}^{-1}$) of conventional electrolyte materials like yttria-stabilized zirconia (YSZ), as well as sluggish electrode reactions resulting from the low catalytic activity (Alipour et al., 2022; Fan et al., 2022; Zhu et al., 2021a). The incorporation or in situ manufacture of active nanocomponents to form the nanocomposite might be a solution to these problems (Mushtaq et al., 2021b; Tabassum et al., 2019). Carbon nanotubes (CNTs) have exhibited superior thermal and electrical conductivity, which accelerates the heat

transfer and increases the reaction rate during electrochemical reactions (Choudhary et al., 2020; Zhang et al., 2020). It was reported that adding multi-wall carbon nanotubes (MWCNTs) to the $\text{Pr}_{0.6}\text{Sr}_{0.4}\text{Fe}_{0.8}\text{Co}_{0.2}\text{O}_3$ (PSFC) perovskite cathode material could adjust the size of nanoparticles, lowering the material's area specific resistance (Pinedo et al., 2011). Moreover, alloying with transition metals could be an efficient method for enhancing catalytic activity to prevent metal particle agglomeration (Cai et al., 2020; Yan et al., 2019). Ju et al. (Lee et al., 2021) developed a bimetallic anode using electrospinning. In comparison to Ni-Fe spherical powder, this fiber anode possessed higher anodic activity and was more resistant to coarsening of metallic particles. However, the fabrication process is complicated and time-consuming.

Catalytic pyrolysis and gasification technologies have been proved to be a feasible and economical route to produce CNTs from waste plastics compared with the traditional methods such as landfill or incineration (Cai et al., 2021; Jie et al., 2020). It is reported 95% of plastic packaging material value (USD 80-120 billion per year) wasted only after the first-use cycle (Dogu et al., 2021) and potential health risks caused by waste plastics have been highlighted (Ostle et al., 2019). Furthermore, the spent catalyst produced during the pyrolysis-catalysis of waste plastics includes not only CNTs but also contaminants. Therefore, it is conventional to remove impurities such as catalyst support and amorphous carbon to preserve the properties of CNTs. However, the CNTs purification rely on various

chemical oxidants, such as KMnO_4 (Azodpour and Baniadam, 2019), leading to high energy consumption and burdensome post-processing. From another standpoint, the intentional utilization of remaining metallic phases in CNTs is a cost-effective and reasonable approach to produce advanced functional carbon/metal composite, especially in the various energy storage systems, including fuel cells and some electrochemical reactions (Biemolt et al., 2021; Campos-Roldán et al., 2020; Mao et al., 2020; Pagliaro et al., 2021). Notably, sufficient contact between metal-based oxides and CNTs must be formed for efficient charge transfer to increase the overall electrocatalytic activities of metal nanoparticles and CNTs. Therefore, in addition to the physical mixture, establishing an intrinsic chemical relationship between CNTs and transition metal is a critical challenge to enhance the charge transfer efficiency between the interfaces of these two components.

Due to the ongoing COVID-19 global pandemic, the use of personal protective equipment (PPE) has witnessed a massive increase (Yuan et al., 2021). The mandatory requirement of single-use face masks in many countries caused the accumulation of waste polypropylene (PP) (Harussani et al., 2021). Herein, we first reported the improvement of LT-SOFC performances via blending well-dispersed non-precious metal nanoparticles encapsulated in CNTs (M@CNTs) in the anode, which was in-line synthesised via one-step directionally catalytic pyrolysis of waste PP (Fig. 1). The influences of the catalyst's active metal components (monometallic Ni, Fe, bimetallic NiFe) on the quality of M@CNTs ,

working mechanism, and the SOFC performances were investigated. This work presents a novel strategy to achieve sustainable management of waste plastics and accelerate the practical applications of LT-SOFCs, achieving the United Nation's Sustainable Development Goals (SDGs), such as mitigating plastic pollution (SDG 14: life below water and SDG 15: life on land) and generating clean energy (SDG 7: renewable energy).

Results

The physicochemical characterization of M@CNTs

After the pyrolysis and catalytic decomposition of PP, a large amount of filamentous carbon generated from all three kinds catalysts (Fig. 2, S1 and S2). The carbon deposits formed on the NiFe@CNTs appeared to be mainly the filamentous carbon with the length of tens of microns (Fig. 2a), while more irregular shapes of the cluster were observed on the Ni@CNTs (Fig. S1a). TEM observations further demonstrated the filamentous carbons were identified as CNTs for all samples. The average size of CNTs outer diameters followed the decreasing order, that is, Ni@CNTs (36.13 ± 6.52 nm) > Fe@CNTs (19.90 ± 4.64 nm) > NiFe@CNTs (14.38 ± 3.84 nm), as displayed in Fig. S1d, S2d, and 2b. Furthermore, the most minor standard deviation was obtained with the NiFe@CNTs, thus it had the better uniform distribution of CNTs that possessed a longer length and less tortuosity among the three samples.

The high-resolution TEM (HRTEM) images displayed that the metallic nanoparticles were trapped inside the bamboo-like multi-walled CNTs (Fig. 2c, d). The metallic nanoparticles were further identified as Fe-Ni alloy by the lattice spacing of 2.07 Å (Fig. 2d), corresponding to the (111) plane and agreed well with the XRD pattern (Fig. 3b). The Fe-Ni alloy had been proved to be the active metallic compound for the formation of CNTs, which was consistent with previous reports (He et al., 2020; Jia et al., 2021). Closer observation showed that the carbon layer spacing of the CNTs outer wall was 0.34 nm (Fig. 2e), which was related to the graphite with the (002) plane. Furthermore, the line profiles in a single particle's high-angle annular dark-field scanning TEM (HAADF-STEM) picture (Fig. 2f) revealed a significantly greater signal for Fe than Ni. NiFe@CNTs was predominantly constituted of C, encapsulating nanoparticles of Fe and Ni, according to the TEM-energy-dispersive X-ray (TEM-EDX) data (Fig. 2g). It's worth noting that the Fe and Ni mappings were almost identical, highlighting the Fe-Ni alloy's synergistic effects in fostering CNT development.

The bimetallic NiFe@CNTs witnessed the second highest surface area of 170.75 m² g⁻¹ and an average pore size of 11.62 nm (Fig. 3a and Table S1). Among the three synthesized nanomaterials, the Ni@CNTs possessed the highest surface area (190.81 m² g⁻¹), associated with the smallest average pore size (10.20 nm). Furthermore, the pore volume of the three samples showed no considerable differences, and their sizes were around 0.50

mL g⁻¹. In addition, the H3 hysteresis loop at relatively high pressure can be determined as type IV for all M@CNTs according to the IUPAC classification, suggesting a mesoporous structure. The corresponding pore size distribution was investigated using the N₂-DFT calculation method, and the results revealed that micropores and mesopores co-existed, indicating a hierarchical architecture. It has been reported that hierarchical architecture can work as an efficient mass in the electrocatalytic process (Huang et al., 2019; Suzuki et al., 2009). In particular, the NiFe@CNTs sample exhibited much transfer channel higher pore volume between 1 and 2 nm, revealing the widespread micropore structure, which could offer abundant electrocatalytic active sites (Meng et al., 2019).

The X-ray diffraction (XRD) patterns in Fig. 3b revealed a distinct intensity signal at about 26° corresponding to graphite carbon (JCPDS #41-1487) for all three samples. For the Ni@CNTs, metallic Ni is detected by the diffraction peak peaks located at $2\theta = 44.51^\circ$, 51.85° and 76.37° , which are related to (111), (200) and (220) planes of nickel (JCPDS #04-0850) respectively (Qin et al., 2021). Nevertheless, Fe₃C was found to be the main component for the Fe@CNTs, which was identified by JCPDS #35-0772 to generate the reflections at 35.23° (200), 43.74° (102) and 44.99° (031) (Wang et al., 2021b). The lack of metallic iron in Fe@CNTs might be ascribed to the combination of iron species and the carbon matrix, leading to the generation of metal carbide. However, nickel carbide (Ni₃C) had not been detected in Ni@CNTs. As a consequence, the carbon solution degree in Fe

can be substantially greater than in Ni, promoting the generation of metal carbide (Pudukudy et al., 2017). This was also confirmed by others work which found the generation of metal carbide promoted the formation of CNTs (Zhou et al., 2017). For the NiFe@CNTs, the Fe-Ni alloy was detected as $\text{Fe}_{0.64}\text{Ni}_{0.36}$ by JCPDS #47-1405 to generate the reflections at 43.60° (111), 50.79° (200) and 74.68° (220) apart from the Fe_3C phase. The XRD results had further verified that Fe-Ni alloy was the direct active site for the growth of CNTs, which agreed with the prevalent understanding of bimetallic Fe-Ni species catalysts proposed by previous work (He et al., 2020; Yao and Wang, 2020). It can be concluded the Fe-Ni alloy's synergistic effect boosted the ability of carbon solutions in metals to increase CNT formation and uniform distribution. Some researchers have reported that the particle size of active sites has some impacts on the size of the CNTs (He et al., 2021; Kotov et al., 2021), therefore the average crystalline size of catalyst was calculated according to Scherrer equation ($D=k\lambda/\beta \cos \theta$). After the WPF refinement, the average crystalline size of Ni, Fe_3C , $\text{Fe}_{0.64}\text{Ni}_{0.36}$, was calculated to be 20.0 nm, 14.5 nm and 12.3 nm, respectively, which displayed the decreasing trend following the order: $\text{Ni@CNTs} > \text{Fe@CNTs} > \text{NiFe@CNTs}$. From the TEM results above, it was found that the same trend was also shown according to the mean size of the outer diameters of CNTs. Therefore, it was the particle size of metal nanoparticles that played a distinct role in the morphology of as-formed CNTs.

TPO analysis of the M@CNTs was conducted to identify the stability of carbon deposits and chemical existence form in Fig. 3c. Compared with the monometallic Ni@CNTs and Fe@CNTs, the starting temperature of weight reduction was higher for NiFe@CNTs, which meant that NiFe@CNTs had better thermal stability than others. Moreover, the derivative thermal gravimetry (DTG) results (Fig. 3c insert) further demonstrated the better stability of NiFe@CNTs because the corresponding weightlessness peak shifted towards the high-temperature zone. That phenomenon revealed that the carbon formed on different samples might have differences between each other. According to the previous research, two kinds of carbon could be detected during the deposition process, and the carbon form could be distinguished by oxidation temperature owing to their different oxidation properties (Liu et al., 2017; Zhang et al., 2015). The weight loss at temperature higher than 550 °C was related to graphite (CNTs here), compared with the oxidation of amorphous carbon at lower temperature. The carbon deposits produced over the NiFe@CNTs exhibited a higher proportion of CNTs than others (Fig. S3). It was calculated that around 363 mg g_{plastic}⁻¹ CNTs concentrated on the NiFe@CNTs, taking over 90% of the carbon deposits.

The surface nature and chemical state of each element of Ni@CNT, Fe@CNTs, and NiFe@CNTs were determined using high-resolution X-ray photoelectron spectroscopy (HRXPS). The Ni 2p spectrum displays two Ni2p_{3/2} and Ni2p_{1/2} areas, which can be

deconvoluted into six peaks in Fig. 3d (Wang et al., 2019b). Thereinto, two peaks at 853 eV and 870 eV are related to metallic Ni species, while the oxidized Ni species are represented by the peaks at 856 eV and 875 eV. Moreover, Fe2p XPS spectra also revealed two chemically different species with broad Fe2p peaks. The two peaks at ~707 eV and ~720 eV in the Fe 2p spectrum could be assigned to Fe₃C (Xiujun Fan, 2015), while the two peaks at ~711 eV and ~725 eV belonged to oxidation states of Fe species. The metallic Ni and Fe peaks appearing in XPS spectra agreed well with XRD analysis and HAADF-STEM results. It was notable that the Ni and Fe peaks shifted to the higher binding energy in NiFe@CNTs (Table S3, S4), respectively. This shift indicated the less charge density on either Ni or Fe atoms, which is a clue of the interaction of Fe-Ni alloy (Loos et al., 2019). The peaks in the C 1s spectra deconvoluted at ~284.8, ~285.3, ~286.41 and ~290.65 eV are attributed to C-C, defects bonds, C-O-C and π - π^* respectively (Fig. S4 and Table S5). Compared with the monometallic M@CNTs, NiFe@CNTs possessed the highest relative content of C-C (56.80%), indicating the strong C-H bond cleavage catalytic activity of Fe-Ni alloy during the thermochemical reactions. However, the proportion of defects for NiFe@CNTs (15.52%) is evidently reduced by half in contrast with Ni@CNTs or Fe@CNTs, indicating the high graphitization structure.

Furthermore, Raman spectra in Fig. 3f revealed three typical peaks appearing at around 1350 cm⁻¹ (D band), 1580 cm⁻¹ (G band) and 2690 cm⁻¹ (G' band) in M@CNTs. They

are linked to amorphous carbon or the defects on the carbon nanotube, the stretching vibration of crystalline graphite and the two-phonon lattice vibration process (Chen et al., 2014; Jiao et al., 2009), respectively. NiFe@CNTs witnessed the least number of defects, since the D band and G band intensity ratios (I_D/I_G) is pretty lower than others, again confirming the high purity of CNTs and in accordance with the results in Fig. S3. Furthermore, the maximum I_G/I_G was observed for NiFe@CNTs of 0.72, also reflecting the higher graphitization degree of the carbon collected. Compared with the other two Fe-containing samples, Ni@CNTs possessed a relatively wide D band, which could be linked to higher complexity, such as the carbon nano onions in layer stacking. The nickel carbide did not form in Ni@CNTs, therefore the carbon saturation occurred in a short time, the carbon atoms began to crystallize, and the first single layered graphene formed over the Ni catalyst particle. The saturation and crystallization would repeat with a constant supply of carbon atoms, and multiple graphene layers grow surrounding the catalyst, resulting in the formation of a carbon nano onion (Dhand et al., 2021).

SOFC performances of M@CNTs

The remarkable properties of carbon nanotubes-transition metal composites garner an increasing interest from the catalysis community. It has been demonstrated that this kind of nanocomposite possessed excellent HOR and ORR electrocatalytic activity for proton

exchange membrane fuel cells (PEMFCs) and rechargeable metal-air batteries (MABs), which are clean power generation devices (Ma et al., 2019). Compared to the conventional SOFCs that can only be operated in a high temperature range (800-1000 °C), the LT-SOFCs with decreased operation temperature (<550 °C) may improve the commercialization prospects of SOFCs. The graphite structure of CNT could be well maintained below 500 °C, as illustrated in the TPO analysis. Hence, the carbon encapsulated metallic particles was utilized as anode electrode expecting improved HOR catalytic activity. The primary components of a fuel cell are an electrolyte, a cathode, and an anode, as shown schematically in Fig. 4a. In this fuel cell configuration, the CeO₂ was used as an electrolyte since it showed an impressive ionic conductivity at low temperature (Wang et al., 2019a; Xing et al., 2019). The I-V curves for fuel cells with the cell structure of NCAL-M@CNTs/CeO₂/NCAL-M@CNTs were shown in Fig. 4b. The maximal power densities for fuel cells with NiFe@CNTs as an anode at 500 °C was 885 mW cm⁻², which was higher than those counterparts with Ni@CNTs and Fe@CNTs-blended anode. Such observation indicated that the cell performance at a low-temperature range was enhanced with the additive of NiFe@CNTs, which could mainly be attributed to the improved electrocatalytic activity of anode. Even when compared with several different anode materials and operating conditions for the performances of SOFCs (Table 1), our sample presents the highest power density (Fig. 4d), no matter whether the operating temperature is higher or

244 lower than 600 °C.

245 **Table 1** Comparisons with several different anode materials and operating conditions for
 246 the performances of SOFCs.

Anode Materials	Power density (mWcm ⁻²)	Temperature (°C)	Electrolyte	Reference
NiFe@CNTs	885	500	CeO ₂	This work
Sr _{0.95} (Ti _{0.3} Fe _{0.63} Ni _{0.07})O _{3-δ} (STFN)	400	700	La _{0.8} Sr _{0.2} Ga _{0.83} Mg _{0.17} O _{3-δ} (LSGM)	(Zhu et al., 2018)
BaZr _{0.1} Ce _{0.7} Y _{0.1} Yb _{0.1} O _{3-δ}	370	500	Samaria doped ceria (SDC)	(Chen et al., 2018)
Al _{0.05} Ni _{0.1} Ti _{0.05} Zn _{0.80} -SDC (ATZN-SDC)	370	650	Samaria doped ceria (SDC)	(Ajmal Khan et al., 2018)
LiNiCuZn-O (LNCZ-O)	455	600	Samaria doped ceria (SDC)	(Khan et al., 2020)
Al _{0.1} Mn _{0.1} Zn _{0.8} O (AMZ)	407	550	Gadolinium doped ceria (GDC)	(Mumtaz et al., 2019)
Al _{0.1} Mn _{0.1} Ni _{0.1} Zn _{0.7} O (AMNZ)	535	550	Gadolinium doped ceria (GDC)	(Mumtaz et al., 2019)
Ni-SDC	508	650	SDC	(Ahsan et al., 2020)
Ni _{0.6} (Ba _{0.3} Ce _{0.2} Zn _{0.5}) _{0.4} (NBCZ)	350	650	Na carbonated samarium doped ceria (NSDC)	(Batoool et al., 2019)
Ag _{0.25} Ti _{0.05} Zn _{0.70} oxide	354	650	SDC	(Hussain et al., 2019)
Mo doped Pr _{0.5} Ba _{0.5} MnO _{3-δ} (Mo-PBMO)	560	800	YSZ	(Sun et al., 2016)
La _{0.3} Sr _{0.7} Fe _{0.7} Ti _{0.3} O ₃ (LSFT)	374	700	Ytria- stabilized zirconia (YSZ)	(Cao et al., 2015)

To further verify the improved electrode kinetics process, the electrochemical impedance spectra (EIS) studies were carried out for fuel cells with different anode additives under cell operation conditions at 500 °C. The results were fitted with an equivalent circuit as presented in Fig. 4c, and the simulated data were summarized in Table S6. R_0 indicates the ohmic resistance in the equivalent circuit, which could be calculated by computing the intercept on the real axis at high frequencies, while R_1 and R_2 represent the electrolyte's border resistances and the electrode's polarization resistance respectively. According to the simulated results for the M@CNTs anode fuel cell, the ohmic resistance decreased from 0.47 to 0.36 $\Omega \text{ cm}^{-2}$, suggesting an improved electrochemical performance in the CNTs-electrode based fuel cell. The hydrogen oxidation reaction and oxygen reduction reaction happened on the sites located at the triple phase boundaries (TPB) in the fuel cell, where involved ions transfer, electrons transfer and molecular species adsorption-desorption process. Molecular was oxidized/reduced into ions on the electrode, generating electrons at the anode side. Ions transferred through the electrolyte, while electrons were conducted to the external circuit. Since we used the same commercial CeO_2 with same ionic conductivity as the electrolyte for all the devices, the ions transfer activation energy of the electrolyte was not the key factor that contributed to performance gains. Accordingly, the catalytic activity of triple-phase-boundary played the key role in the enhanced fuel cell performance. The cell with NiFe@CNTs as electrode expressed the lower polarization

resistance at 500 °C, compared with Ni@CNTs and Fe@CNTs, ascribing to the high electrode catalytic activity, which arose from the encapsulated metallic particles with surface carbon mentioned above. The distinctive structure of the produced nanocomposite, in which the alloy particles were encased by CNTs, may account for the decreased polarization resistance of NiFe@CNTs, leading to the charge redistribution between the interface and fast charge transfer. The electronic property of metal core was modulated by the CNTs coupling to optimize HOR/ORR activity of M@CNTs catalysts.

Discussion

DFT calculations were employed to deeply investigate the effects of the different metal species (mono Ni, Fe and bimetallic NiFe) of M@CNTs on the HOR activity, since HOR, as the half-reaction, played a vital role in SOFC performance (Zhu et al., 2021b). According to the XRD and TEM results above, Ni, Fe₃C, Fe_{0.64}Ni_{0.36}, have been referred to as the active species of Ni@CNTs, Fe @CNTs and NiFe@CNTs, respectively. Furthermore, Ni has been found to expose the (111), (200) and (220) facets, and its space group is Fm3m (225). Fe₃C exists in Fe@CNTs, exposing the (200), (102) and (031) facets, and its space group is Pnma (62), while Fe_{0.64}Ni_{0.36} in NiFe@CNTs, exposing the (111), (200) and (220) facets, and its space group is Fm3m (225). The possible elementary steps comprising the HOR are $\frac{1}{2}\text{H}_2 \rightarrow \text{H}^*$ and $\text{H}^* \rightarrow \text{H}^+$.

Appropriate hydrogen adsorption energy is significant in the catalytic activity according to the Sabatier volcano relationship (Mao et al., 2020). Therefore, the hydrogen adsorption energy of different binding modes was calculated. Firstly, we investigated the effects of the different active sites of the nanoparticles, especially at the edge of the cluster. As shown in Fig. 5a, the 234 hollow site was the preferential hydrogen adsorption site of all studied bonds for Ni@CNTs compared with the 123 hollow site or the 45 bridge site. However, as for Fe@CNTs, the 12 bridge site possessed the lowest hydrogen adsorption energy of 0.11 eV, which was possibly attributed to the introduction of C atom in the Fe₃C nanoparticles (Fig. 5b). It was noteworthy that an optimal near zero value of hydrogen adsorption energy was obtained at the hollow site of 456 when NiFe alloy forms in the NiFe@CNTs (Fig. 5c), further indicating the synergetic effects of bimetallic Fe-Ni species during the catalytic synthesis of NiFe@CNTs. Similar results have been reported for the bimetallic phosphide (Fe_{0.3}Co_{0.7}P@CNTs) nanocomposite. It was concluded that the free energy of H adsorption closer to zero, larger binding strength for H₂O and higher electrical conductivity contributed to the enhanced catalytic activities of Fe_{0.3}Co_{0.7}P (Wang et al., 2021a).

Furthermore, the entire processes of HOR on the three different kinds of M@CNTs were further investigated (Fig. 5d). The results revealed that the different species of metal nanoparticles had significant influences on the HOR activity of catalysts. The bimetallic

NiFe@CNTs had the smallest energy barrier among the whole reaction process, followed by Fe@CNTs and Ni@CNTs, being consistent with the trend of SOFC performance. To reveal an electronic correlation between the metallic ions and graphene, the ultraviolet photoemission spectroscopy measurements were performed, and the data were depicted in Fig. 5e. The work function of graphene was increased from 5.05 eV to 5.72 eV and 6.60 eV for NiFe@CNTs, Fe@CNTs and Ni@CNTs, respectively. The downward shift of work function indicates an improved charge transfer from CNTs to metal ions, thus increasing the HOR catalytic activity of NiFe@CNTs for LT-SOFCs (Kwon et al., 2012).

Conclusions

CNTs materials, with non-precious transition metal nanoparticles encapsulated in, were successfully synthesized to enhance the LT-SOFC performances from one step of pyrolysis and in-line catalytic decomposition of polypropylene. Compared with monometallic Ni and Fe, the CNTs generated from bimetallic (NiFe@CNTs) revealed longer, smoother and narrower CNTs and well-dispersed Fe-Ni alloy nanoparticles could be seen inside simultaneously. Both carbon peak that was closed to the theoretical one and lower I_D/I_G ratio proved the high graphitization structure of the CNTs collected. NiFe@CNTs exhibited remarkable low-temperature SOFC performance as an electrode additive with a maximum power density of 885 mW cm^{-2} at 500°C , and this is mainly due

to the efficient agglomeration prevention and electrical conductivity. DFT calculations also demonstrated that an optimal near zero value of hydrogen adsorption energy was obtained at the hollow site of 456 when NiFe alloy forms in the NiFe@CNTs. This research not only sets the path for a new approach to economically and ecologically recycle plastic waste, but it also shines light on low-cost and high-performance catalysts for LT-SOFCs with tunable bimetallic-species-loaded carbon-based materials.

Limitations of the study

The impurities in plastics are not considered in this study. We will use real-world waste plastics to prepare carbon-based nanocomposites and further verify their SOFC performances. The life-cycle analysis and techno-economic analysis could also be introduced to accelerate industrialization in the future.

Resource availability

Lead Contact

Further information and requests for resources and reagents should be directed to and will be fulfilled by the Lead Contact, Huiyan Zhang (hyzhang@seu.edu.cn).

Materials Availability

This study did not generate new unique reagents.

Data and Code Availability

- All data are available in the paper and in supplemental information, and/or from the corresponding author upon reasonable request.
- This paper does not report original codes.
- Any additional information required to reanalyze the data reported in this paper is available from the lead contact upon request.

Experimental model and subject details

This work did not need any unique experimental model.

Method details

Production of the synthesized nanocomposite

Ni/Al₂O₃, Fe/Al₂O₃, NiFe/Al₂O₃ were firstly prepared by a single-step sol-gel method, respectively. All catalysts contained approximately 10 wt.% of active metals. In NiFe/Al₂O₃, the Ni to Fe molar ratio was controlled at 1:3. For the synthesis of the catalysts, 40 g aluminum tri-sec-butoxide (C₁₂H₂₇AlO₃, AR 97%, Aladdin) was dissolved in 300 ml ethanol and stirred for 2.5 h at 80 °C. Then, the pre-dissolved active metal precursor mixture with nickel nitrate hexahydrate (Ni (NO₃)₂·6H₂O, AR 98%, Aladdin, if required), iron (III) nitrate nonahydrate (Fe (NO₃)₃·9H₂O, AR ≥ 98.50%, Sinopharm Chemical

Reagent Co. Ltd., if required), and 5 ml deionized water was added drop by drop. For example, taking the bimetallic catalyst NiFe/Al₂O₃, 4.93g Fe (NO₃)₃·9H₂O and 1.18g Ni (NO₃)₂·6H₂O were added, allowing the Ni to Fe molar ratio to be 1:3. Subsequently, the mixture was stirred for 0.5 h and dried at 80 °C overnight. Finally, the gel was sieved to 80-100 mesh and calcined at 850 °C for 3 h in air. Notably, here in this work, typical waste PP was selected as plastic feedstock. Table S7 showed the ultimate analysis and proximate analysis of PP.

The preparation of CNTs encapsulated Ni- and Fe- based nanoparticles was conducted in a two-stage fixed-bed system (Fig. S5). The upper zone (Zone I) was used for PP pyrolysis, while the bottom zone (Zone II) was used for further catalytic decomposition of generated volatiles, making carbon nanomaterials deposit on the catalyst. The inner diameter and length of upper reactor was 26 mm and 300 mm, while bottom reactor was 18 mm and 300 mm. 1g of PP was loaded within a basket hanging in the middle of zone I and 0.25 g of catalyst were placed in the center of zone II in a typical experiment. The system was purged with 50 mL min⁻¹ N₂ for 10 mins. Zone II was pre-heated to 800 °C and kept stable until the experiment finished. When zone II reached the designed temperature, zone I started to heat up to 500 °C within 30 min and then was kept stable at 500 °C for an additional 20 minutes to make sure the complete reaction. After a typical test, the CNTs encapsulated Ni- and Fe- based nanoparticles would be successfully synthesized in Zone

II. The obtained samples were respectively denoted as Ni@CNTs, Fe@CNTs, NiFe@CNTs hereafter.

Characterizations

The specific surface area of fresh catalysts was evaluated using the Brunauer-Emmett-Teller (BET) equation and measured at 77 K on an ASAP 2020 (Micromeritics, USA). The reducibility of fresh catalysts was measured by temperature programmed reduction (TPR) in a Micromeritics AutoChem. To be precise, around 10 mg catalyst was heated to 850 °C in a flowing gas of 10 vol% H₂ (2.231 mmol min⁻¹, balanced by Ar) with a heating rate of 10 °C min⁻¹. High-resolution X-ray photoelectron spectroscopy (HRXPS) was used to examine the surface chemical compositions of fresh catalysts with an Al K line (15 kV, 10 mA, 150 W) as a radiation source (250 Xi, Thermo ESCALAB). The thermogravimetric analyzer (Discovery TG55) was used to conduct temperature programmed oxidation (TPO) distinguishing the type of carbon, such as amorphous carbon or graphite, on the spent catalysts. ~10 mg of sample was held at 105 °C for 30 min to remove moisture and then heated to 800 °C with the ramping rate of 10 °C min⁻¹ in an air atmosphere (100 ml min⁻¹). An X-ray diffraction equipment (XRD, smartlab9) was employed to investigate the crystal phases. It was operated at 40 kV and 150 mA ($\lambda = 0.15406$ nm) with an angle reflection between 5° and 85°. The XRD scanning rate was 8° min⁻¹. The morphology of samples was observed both with a scanning electron microscope (SEM, Ultra Plus) and a high-resolution

transmission electron microscope (HRTEM, JEOL JEM-2100F). HAADF-STEM cross-sectional compositional profiles of samples were investigated by a high-resolution transmission electron microscope (HRTEM, JEOL JEM-2100F). The Raman spectrometer was employed to investigate the graphitization of carbon gathered. Raman shift was between 200 and 3500 cm^{-1} at a wavelength of 532 nm. In addition, valence band level maximums were measured by ultraviolet photoelectron spectroscopy (UPS) with a 100 MeV total instrumental energy resolution (Thermofisher escalab 250xi).

SOFC fabrication and tests

The schematic diagram of the SOFC fabrication process was shown in Fig. S6. The commercial $\text{LiNi}_{0.8}\text{Co}_{0.15}\text{Al}_{0.05}$ (NCAL) material is commonly utilized as the electrode of ceramic fuel cells (CFCs). NCAL mixed with Ni@CNTs, Fe@CNTs and NiFe@CNTs in a 1:0.1 weight ratio was developed to further explore its catalyst function in a low-temperature range. They were homogeneously blended in the mortar with ethanol and terpineol (1:1 volume ratio). Then, the mixed slurry was smeared on Ni foam and the foam was put into an oven at 120 °C for 1h to remove the additional organic solvent, which was used as an electrode and current collector. For comparison purposes, the devices based on CeO_2 electrolyte and different electrodes were fabricated by one-step pressing under 8 Mpa pressure for 60 s to obtain the pellet. The resulting fuel cell devices were labeled as NCAL-Ni@CNTs/ CeO_2 /NCAL-Ni@CNTs, NCAL-Fe@CNTs/ CeO_2 /NCAL-Fe@CNTs and

NCAL-NiFe@CNTs/CeO₂/NCAL-NiFe@CNTs. They are roughly 2 mm in thickness and 13 mm in diameter. The cells were pre-heated in the testing setup at 500 °C for 1 h. The SOFCs performance measurements were conducted on an electronic load instrument (IT8511, ITECH Electrical Co., Ltd., Nanjing, China) at 500 °C. The pure hydrogen (99.999%) was used as fuel with a flow rate of 100 mL min⁻¹) while air as the oxidant with a flow rate of 100 mL min⁻¹.

Computational method

The Vienna Ab initio Simulation Package (VASP) was used to perform all density functional theory (DFT) computations using the Perdew-Burke-Ernzerhof (PBE) functional under the generalized gradient approximation (GGA) (Nie et al., 2018). The projected augmented wave (PAW) potentials were chosen to describe the ionic cores. The valence electrons were introduced based on a plane wave basis set with a kinetic energy cutoff of 400 eV (Zhang et al., 2021a). The force convergence was determined to be smaller than 0.05 eV Å⁻¹ to perform geometry optimizations. Spin-polarized effect and van der Waals force correction were both considered in all calculations. Previous studies have proved that the curvature of the CNT support could be almost ignored owing to the comparatively large size of both the CNTs and the encapsulated metal nanoparticles; as a result, the CNT support was approximated with a graphene sheet to simplify the model's complexity (Popov, 2004). The graphene layer was built with the periodicity of p (6×6)

(72 C atoms). Nanoparticles of Ni (13 Ni atoms), Fe₃C (9 Fe atoms and 4 C atoms) and Fe_{0.64}Ni_{0.36} (9 Fe atoms and 4 Ni atoms) were built on the carbon layer, describing the structure of M@CNTs. All the surface calculations were conducted using Monkhorst-Pack k-points of 2×2×1. This allowed a certain nanoparticle to be placed on graphene while allowing both the nanoparticle and the support to relax. The standard free energies corrections were used to obtain the free energy at 500 °C (Cao et al., 2011).

Quantification and statistical analysis

Our study doesn't include quantification or statistical analysis.

Additional resources

Our study has not generated or contributed to a new website/forum or not been part of a clinical trial.

Acknowledgements

This work was supported by the National Nature Science Fund for Excellent Young Scholar of China (Grant No. 51822604), Scientific Research Foundation of Southeast University Graduate School (YBPY2007) and China Scholarship Council (202006090329).

Author contributions

Conceptualization, Q. Y. L. and H. Y. Z.; Methodology, Q. Y. L., H. Y. Z., and F. Z.

W.; Writing-original draft, Q. Y. L. and F. Z. W.; Writing-review & editing, Q. Y. L., H. Y. Z., X. Z. Y., and X. B. C.; Data curation, F. Z. W., E. Y. H., and R. H.; Software, F. Z. W. and E. Y. H.; Visualization, T. L., N. C., and X. Z. Y.; Investigation, E. Y. H., T. L., and R. H.; Funding Acquisition, H. Y. Z.; Supervision, H. Y. Z. and R. X.

Declaration of interests

The authors declare no competing interest.

Supplemental information

Fig. S1 to S6

Table S1 to S7

References

- Ahsan, M., Irshad, M., Fu, P.F., Siraj, K., Raza, R., and Javed, F. (2020). The effect of calcination temperature on the properties of Ni-SDC cermet anode. *Ceram. Int.* *46*, 2780-2785. 10.1016/j.ceramint.2019.09.268.
- Ajmal Khan, M., Xu, C., Song, Z., Raza, R., Ahmad, M.A., Abbas, G., and Zhu, B. (2018). Synthesize and characterization of ceria based nano-composite materials for low temperature solid oxide fuel cell. *Int. J. Hydrogen Energy* *43*, 6310-6317. 10.1016/j.ijhydene.2018.01.166.
- Alipour, S., Sagir, E., and Sadeghi, A. (2022). Multi-criteria decision-making approach assisting to select materials for low-temperature solid oxide fuel cell: Electrolyte, cathode& anode. *Int. J. Hydrogen Energy* *47*, 19810-19820. 10.1016/j.ijhydene.2022.02.095.
- Azodpour, J., and Baniadam, M. (2019). Microwave assisted purification of multi-walled carbon nanotubes by potassium permanganate; effect of acid to oxidant molar ratio and treatment time. *Diamond Relat. Mater.* *98*, 107485. 10.1016/j.diamond.2019.107485.
- Batool, R., Gill, R., Altaf, F., Ahmad, M.A., Raza, R., Khan, M.A., Hussain, F., Rehman, Z.u., and Abbas, G. (2019). Structural and electrochemical study of $\text{Ba}_{0.15}\text{Cu}_{0.15}\text{Ni}_{0.10}\text{Zn}_{0.60}$ oxide anode for low temperature solid oxide fuel cell. *J. Alloys Compd.* *780*, 653-659. 10.1016/j.jallcom.2018.11.392.

Biemolt, J., Douglin, J.C., Singh, R.K., Davydova, E.S., Yan, N., Rothenberg, G., and Dekel, D.R. (2021). An anion-exchange membrane fuel cell containing only abundant and affordable materials. *Energy Technol.* 9, 2000909. 10.1002/ente.202000909.

Cai, N., Li, X., Xia, S., Sun, L., Hu, J., Bartocci, P., Fantozzi, F., Williams, P.T., Yang, H., and Chen, H. (2021). Pyrolysis-catalysis of different waste plastics over Fe/Al₂O₃ catalyst: High-value hydrogen, liquid fuels, carbon nanotubes and possible reaction mechanisms. *Energy Convers. Manage.* 229, 113794. 10.1016/j.enconman.2020.113794.

Cai, N., Xia, S., Zhang, X., Meng, Z., Bartocci, P., Fantozzi, F., Chen, Y., Chen, H., Williams, P.T., and Yang, H. (2020). Preparation of Iron- and Nitrogen-Codoped Carbon Nanotubes from Waste Plastics Pyrolysis for the Oxygen Reduction Reaction. *ChemSusChem* 13, 938-944. 10.1002/cssc.201903293.

Campos-Roldán, C.A., Calvillo, L., Boaro, M., de Guadalupe González-Huerta, R., Granozzi, G., and Alonso-Vante, N. (2020). NiO–Ni/CNT as an efficient hydrogen electrode catalyst for a unitized regenerative alkaline microfluidic cell. *ACS Appl. Energy Mater.* 3, 4746-4755. 10.1021/acsaem.0c00375.

Cao, X.M., Burch, R., Hardacre, C., and Hu, P. (2011). An understanding of chemoselective hydrogenation on crotonaldehyde over Pt(1 1 1) in the free energy landscape: The microkinetics study based on first-principles calculations. *Catal. Today* 165, 71-79.

- 505 Cao, Z., Zhang, Y., Miao, J., Wang, Z., Lü, Z., Sui, Y., Huang, X., and Jiang, W. (2015).
 506 Titanium-substituted lanthanum strontium ferrite as a novel electrode material for
 507 symmetrical solid oxide fuel cell. *Int. J. Hydrogen Energy* 40, 16572-16577.
 508 10.1016/j.ijhydene.2015.10.010.
- 509 Chen, C., Hayazawa, N., and Kawata, S. (2014). A 1.7 nm resolution chemical
 510 analysis of carbon nanotubes by tip-enhanced Raman imaging in the ambient. *Nat.*
 511 *Commun.* 5, 3312. 10.1038/ncomms4312.
- 512 Chen, Y., deGlee, B., Tang, Y., Wang, Z., Zhao, B., Wei, Y., Zhang, L., Yoo, S., Pei,
 513 K., Kim, J.H., *et al.* (2018). A robust fuel cell operated on nearly dry methane at 500 °C
 514 enabled by synergistic thermal catalysis and electrocatalysis. *Nat. Energy* 3, 1042-1050.
 515 10.1038/s41560-018-0262-5.
- 516 Choudhary, H.K., Kumar, R., Pawar, S.P., Sundararaj, U., and Sahoo, B. (2020). Effect
 517 of morphology and role of conductivity of embedded metallic nanoparticles on
 518 electromagnetic interference shielding of PVDF-carbonaceous-nanofiller composites.
 519 *Carbon* 164, 357-368. 10.1016/j.carbon.2020.04.007.
- 520 Dhand, V., Yadav, M., Kim, S.H., and Rhee, K.Y. (2021). A comprehensive review on
 521 the prospects of multi-functional carbon nano onions as an effective, high- performance
 522 energy storage material. *Carbon* 175, 534-575. 10.1016/j.carbon.2020.12.083.
- 523 Dogu, O., Pelucchi, M., Van de Vijver, R., Van Steenberge, P.H.M., D'Hooze, D.R.,

- 524 Cuoci, A., Mehl, M., Frassoldati, A., Faravelli, T., and Van Geem, K.M. (2021). The
525 chemistry of chemical recycling of solid plastic waste via pyrolysis and gasification: State-
526 of-the-art, challenges, and future directions. *Prog. Energy Combust. Sci.* 84, 100901.
527 10.1016/j.pecs.2020.100901.
- 528 Fan, Q., Yan, S., and Wang, H. (2022). Nanoscale redox reaction unlocking the next-
529 generation low temperature fuel cell. *Energy Materials*. 10.20517/energymater.2021.26.
- 530 Harussani, M.M., Sapuan, S.M., Rashid, U., Khalina, A., and Ilyas, R.A. (2021).
531 Pyrolysis of polypropylene plastic waste into carbonaceous char: Priority of plastic waste
532 management amidst COVID-19 pandemic. *Sci. Total Environ.* 803, 149911.
533 10.1016/j.scitotenv.2021.149911.
- 534 He, L., Hu, S., Yin, X., Xu, J., Han, H., Li, H., Ren, Q., Su, S., Wang, Y., and Xiang,
535 J. (2020). Promoting effects of Fe-Ni alloy on co-production of H₂ and carbon nanotubes
536 during steam reforming of biomass tar over Ni-Fe/ α -Al₂O₃. *Fuel* 276, 118116.
537 10.1016/j.fuel.2020.118116.
- 538 He, S., Xu, Y., Zhang, Y., Bell, S., and Wu, C. (2021). Waste plastics recycling for
539 producing high-value carbon nanotubes: Investigation of the influence of Manganese
540 content in Fe-based catalysts. *J. Hazard. Mater.* 402, 123726.
541 10.1016/j.jhazmat.2020.123726.
- 542 Hu, E., Jiang, Z., Fan, L., Singh, M., Wang, F., Raza, R., Sajid, M., Wang, J., Kim,

- 543 J.S., and Zhu, B. (2021). Junction and energy band on novel semiconductor-based fuel cells.
544 iScience 24, 102191. 10.1016/j.isci.2021.102191.
- 545 Huang, X., Shen, T., Zhang, T., Qiu, H., Gu, X., Ali, Z., and Hou, Y. (2019). Efficient
546 oxygen reduction catalysts of porous carbon nanostructures decorated with transition metal
547 species. Adv. Energy Mater. 10, 1900375. 10.1002/aenm.201900375.
- 548 Hussain, F., Abbas, G., Ashfaq Ahmad, M., Raza, R., Rehman, Z.U., Mumtaz, S.,
549 Akbar, M., Riaz, R.A., and Dilshad, S. (2019). Comparative electrochemical investigation
550 of zinc based nano-composite anode materials for solid oxide fuel cell. Ceram. Int. 45,
551 1077-1083. 10.1016/j.ceramint.2018.09.288.
- 552 Jia, J., Veksha, A., Lim, T.T., and Lisak, G. (2021). Weakening the strong Fe-La
553 interaction in A-site-deficient perovskite via Ni substitution to promote the thermocatalytic
554 synthesis of carbon nanotubes from plastics. J. Hazard. Mater. 403, 123642.
555 10.1016/j.jhazmat.2020.123642.
- 556 Jiao, L., Zhang, L., Wang, X., Diankov, G., and Dai, H. (2009). Narrow graphene
557 nanoribbons from carbon nanotubes. Nature 458, 877-880. 10.1038/nature07919.
- 558 Jie, X., Li, W., Slocombe, D., Gao, Y., Banerjee, I., Gonzalez-Cortes, S., Yao, B.,
559 AlMegren, H., Alshihri, S., Dilworth, J., *et al.* (2020). Microwave-initiated catalytic
560 deconstruction of plastic waste into hydrogen and high-value carbons. Nat. Catal. 3, 902-
561 912. 10.1038/s41929-020-00518-5.

Khan, S., Majid, A., and Raza, R. (2020). The influence of activated carbon as an additive in anode materials for low temperature solid oxide fuel cells. *Ceram. Int.* *46*, 592-597. 10.1016/j.ceramint.2019.09.007.

Kotov, V., Sviatenko, A., Nebesnyi, A., Filonenko, D., Khovavko, A., and Bondarenko, B. (2021). CNTs growth on reduced iron. *Mater. Today: Proc.* *35*, 616-620. 10.1016/j.matpr.2019.11.287.

Kwon, K.C., Choi, K.S., and Kim, S.Y. (2012). Increased work function in few-Layer graphene sheets via metal chloride doping. *Adv. Funct. Mater.* *22*, 4724-4731. 10.1002/adfm.201200997.

Lee, S., Park, J.H., Lee, K.T., and Ju, Y.-W. (2021). Anodic properties of Ni-Fe bimetallic nanofiber for solid oxide fuel cell using LaGaO₃ electrolyte. *J. Alloys Compd.* *875*, 159911. 10.1016/j.jallcom.2021.159911.

Liu, X., Sun, H., Wu, C., Patel, D., and Huang, J. (2017). Thermal chemical conversion of high-Density polyethylene for the production of valuable carbon nanotubes using Ni/AAO Membrane Catalyst. *Energy Fuels* *32*, 4511-4520. 10.1021/acs.energyfuels.7b03160.

Loos, S., Zaharieva, I., Chernev, P., Lissner, A., and Dau, H. (2019). Electromodified NiFe alloys as electrocatalysts for water oxidation: mechanistic implications of time-resolved UV/Vis tracking of oxidation state changes. *Chemsuschem* *12*, 1966-1976.

581 10.1002/cssc.201802737.

582 Ma, R., Lin, G., Zhou, Y., Liu, Q., Zhang, T., Shan, G., Yang, M., and Wang, J. (2019).
 583 A review of oxygen reduction mechanisms for metal-free carbon-based electrocatalysts.
 584 npj Comput. Mater. 5. 10.1038/s41524-019-0210-3.

585 Mao, J., He, C.T., Pei, J., Liu, Y., Li, J., Chen, W., He, D., Wang, D., and Li, Y. (2020).
 586 Isolated Ni atoms dispersed on Ru nanosheets: High-performance electrocatalysts toward
 587 hydrogen oxidation reaction. Nano Lett. 20, 3442-3448. 10.1021/acs.nanolett.0c00364.

588 Meng, Z., Cai, S., Wang, R., Tang, H., Song, S., and Tsiakaras, P. (2019). Bimetallic-
 589 organic framework-derived hierarchically porous Co-Zn-N-C as efficient catalyst for acidic
 590 oxygen reduction reaction. Appl. Catal., B 244, 120-127. 10.1016/j.apcatb.2018.11.037.

591 Mumtaz, S., Ahmad, M.A., Raza, R., Khan, M.A., Ashiq, M.N., and Abbas, G. (2019).
 592 Nanostructured anode materials for low temperature solid oxide fuel cells: Synthesis and
 593 electrochemical characterizations. Ceram. Int. 45, 21688-21697.
 594 10.1016/j.ceramint.2019.07.169.

595 Mushtaq, N., Lu, Y., Xia, C., Dong, W., Wang, B., Shah, M.A.K.Y., Rauf, S., Akbar,
 596 M., Hu, E., Raza, R., *et al.* (2021a). Promoted electrocatalytic activity and ionic transport
 597 simultaneously in dual functional Ba_{0.5}Sr_{0.5}Fe_{0.8}Sb_{0.2}O_{3-δ}-Sm_{0.2}Ce_{0.8}O_{2-δ} heterostructure.
 598 Appl. Catal., B 298, 120503. 10.1016/j.apcatb.2021.120503.

599 Mushtaq, N., Lu, Y., Xia, C., Dong, W., Wang, B., Wang, X., Yousaf Shah, M.A.K.,

- 600 Rauf, S., Jingjing, N., Hu, E., *et al.* (2021b). Design principle and assessing the correlations
601 in Sb-doped Ba_{0.5}Sr_{0.5}FeO_{3-δ} perovskite oxide for enhanced oxygen reduction catalytic
602 performance. *J. Catal.* *395*, 168-177. 10.1016/j.jcat.2020.12.005.
- 603 Nie, X., Jiang, X., Wang, H., Luo, W., Janik, M.J., Chen, Y., Guo, X., and Song, C.
604 (2018). Mechanistic understanding of alloy effect and water promotion for Pd-Cu
605 bimetallic catalysts in CO₂ hydrogenation to methanol. *ACS Catalysis* *8*, 4873-4892.
606 10.1021/acscatal.7b04150.
- 607 Ostle, C., Thompson, R.C., Broughton, D., Gregory, L., Wootton, M., and Johns, D.G.
608 (2019). The rise in ocean plastics evidenced from a 60-year time series. *Nat. Commun.* *10*,
609 1622. 10.1038/s41467-019-09506-1.
- 610 Pagliaro, M.V., Miller, H.A., Evangelisti, C., Bellini, M., Tuci, G., Pham-Huu, C.,
611 Giambastiani, G., Marelli, M., and Vizza, F. (2021). Synergy between nickel nanoparticles
612 and N-enriched carbon nanotubes enhances alkaline hydrogen oxidation and evolution
613 activity. *ACS Appl. Nano Mater.* *4*, 3586-3596. 10.1021/acsanm.1c00118.
- 614 Pinedo, R., Ruiz de Larramendi, I., Jimenez de Aberasturi, D., Gil de Muro, I., Aguayo,
615 A.T., Ruiz de Larramendi, J.I., and Rojo, T. (2011). A straightforward synthesis of carbon
616 nanotube-perovskite composites for solid oxide fuel cells. *J. Mater. Chem.* *21*, 10273.
617 10.1039/c1jm11632k.
- 618 Popov, V.N. (2004). Curvature effects on the structural, electronic and optical

619 properties of isolated single-walled carbon nanotubes within a symmetry-adapted non-
 620 orthogonal tight-binding model. *NJPh* 6, 17. 10.1088/1367-2630/6/1/017.

621 Pudukudy, M., Yaakob, Z., Mazuki, M.Z., Takriff, M.S., and Jahaya, S.S. (2017). One-
 622 pot sol-gel synthesis of MgO nanoparticles supported nickel and iron catalysts for undiluted
 623 methane decomposition into CO_x free hydrogen and nanocarbon. *Appl. Catal., B* 218, 298-
 624 316. 10.1016/j.apcatb.2017.04.070.

625 Qin, M., Zhang, L., Zhao, X., and Wu, H. (2021). Lightweight Ni Foam - Based
 626 Ultra - Broadband Electromagnetic Wave Absorber. *Adv. Funct. Mater.* 31, 2103436.
 627 10.1002/adfm.202103436.

628 Sun, Y.-F., Zhang, Y.-Q., Hua, B., Behnamian, Y., Li, J., Cui, S.-H., Li, J.-H., and Luo,
 629 J.-L. (2016). Molybdenum doped Pr_{0.5}Ba_{0.5}MnO_{3-δ} (Mo-PBMO) double perovskite as a
 630 potential solid oxide fuel cell anode material. *J. Power Sources* 301, 237-241.
 631 10.1016/j.jpowsour.2015.09.127.

632 Suzuki, T., Hasan, Z., Funahashi, Y., Yamaguchi, T., Fujishiro, Y., and Awano, M.
 633 (2009). Impact of anode microstructure on solid oxide fuel cells. *Science* 325, 852-855.
 634 10.1126/science.1176404.

635 Tabassum, H., Mahmood, A., Zhu, B., Liang, Z., Zhong, R., Guo, S., and Zou, R.
 636 (2019). Recent advances in confining metal-based nanoparticles into carbon nanotubes for
 637 electrochemical energy conversion and storage devices. *Energy Environ. Sci.* 12, 2924-

638 2956. 10.1039/c9ee00315k.

639 Wang, B., Chen, Y., Wu, Q., Lu, Y., Zhang, X., Wang, X., Yu, B., Yang, D., and Zhang,
640 W. (2021a). A co-coordination strategy to realize janus-type bimetallic phosphide as highly
641 efficient and durable bifunctional catalyst for water splitting. *J. Mater. Sci. Technol.* *74*, 11-
642 20. 10.1016/j.jmst.2020.10.009.

643 Wang, B., Zhu, B., Yun, S., Zhang, W., Xia, C., Afzal, M., Cai, Y., Liu, Y., Wang, Y.,
644 and Wang, H. (2019a). Fast ionic conduction in semiconductor $\text{CeO}_{2-\delta}$ electrolyte fuel cells.
645 *NPG Asia Mater.* *11*. 10.1038/s41427-019-0152-8.

646 Wang, C., Yang, H., Zhang, Y., and Wang, Q. (2019b). NiFe alloy nanoparticles with
647 hcp crystal structure stimulate superior oxygen evolution reaction electrocatalytic activity.
648 *Angew. Chem., Int. Ed.* *58*, 6099-6103. 10.1002/anie.201902446.

649 Wang, Y., Li, W., Li, H., Ye, M., Zhang, X., Gong, C., Zhang, H., Wang, G., Zhang,
650 Y., and Yu, C. (2021b). Fe/Fe₃C@CNTs anchored on carbonized wood as both self-standing
651 anode and cathode for synergistic electro-Fenton oxidation and sequestration of As(III).
652 *Chem. Eng. J.* *414*, 128925. 10.1016/j.cej.2021.128925.

653 Xing, Y., Wu, Y., Li, L., Shi, Q., Shi, J., Yun, S., Akbar, M., Wang, B., Kim, J.-S., and
654 Zhu, B. (2019). Proton Shuttles in $\text{CeO}_2/\text{CeO}_{2-\delta}$ core-shell structure. *ACS Energy Lett.* *4*,
655 2601-2607. 10.1021/acsenerylett.9b01829.

656 Xiujun Fan, Z.P., Ruquan Ye, Haiqing Zhou, Xia Guo (2015). M_3C (M: Fe, Co, Ni)

- 657 nanocrystals encased in graphene nanoribbons: An active and stable bifunctional
658 electrocatalyst for oxygen reduction and hydrogen evolution reactions. *ACS Nano* 9, 7407-
659 7418.
- 660 Yan, X.H., Prabhu, P., Xu, H., Meng, Z., Xue, T., and Lee, J.M. (2019). Recent
661 progress of metal carbides encapsulated in carbon - based materials for electrocatalysis of
662 oxygen reduction reaction. *Small Methods* 4, 1900575. 10.1002/smt.201900575.
- 663 Yao, D., and Wang, C.-H. (2020). Pyrolysis and in-line catalytic decomposition of
664 polypropylene to carbon nanomaterials and hydrogen over Fe- and Ni-based catalysts. *Appl.*
665 *Energy* 265, 114819. 10.1016/j.apenergy.2020.114819.
- 666 Yuan, X., Wang, X., Sarkar, B., and Ok, Y.S. (2021). The COVID-19 pandemic
667 necessitates a shift to a plastic circular economy. *Nat. Rev. Earth Environ.* 2, 1-2.
668 10.1038/s43017-021-00223-2.
- 669 Zhang, X., Bi, F., Zhu, Z., Yang, Y., Zhao, S., Chen, J., Lv, X., Wang, Y., Xu, J., and
670 Liu, N. (2021a). The promoting effect of H₂O on rod-like MnCeO_x derived from MOFs
671 for toluene oxidation: A combined experimental and theoretical investigation. *Appl. Catal.,*
672 *B* 297, 120393. 10.1016/j.apcatb.2021.120393.
- 673 Zhang, Y., Chen, B., Guan, D., Xu, M., Ran, R., Ni, M., Zhou, W., O'Hayre, R., and
674 Shao, Z. (2021b). Thermal-expansion offset for high-performance fuel cell cathodes.
675 *Nature* 591, 246-251. 10.1038/s41586-021-03264-1.

Zhang, Y., Wang, L., Xu, H., Cao, J., Chen, D., and Han, W. (2020). 3D chemical cross-linking structure of black phosphorus@CNTs hybrid as a promising anode material for lithium ion batteries. *Adv. Funct. Mater.* *30*, 1909372. 10.1002/adfm.201909372.

Zhang, Y., Wu, C., Nahil, M.A., and Williams, P. (2015). Pyrolysis–catalytic reforming/gasification of waste tires for production of carbon nanotubes and hydrogen. *Energy Fuels* *29*, 3328-3334. 10.1021/acs.energyfuels.5b00408.

Zhou, L., Enakonda, L.R., Harb, M., Saih, Y., Aguilar-Tapia, A., Ould-Chikh, S., Hazemann, J.-l., Li, J., Wei, N., Gary, D., *et al.* (2017). Fe catalysts for methane decomposition to produce hydrogen and carbon nano materials. *Appl. Catal., B* *208*, 44-59. 10.1016/j.apcatb.2017.02.052.

Zhu, B., Fan, L., Mushtaq, N., Raza, R., Sajid, M., Wu, Y., Lin, W., Kim, J.-S., Lund, P.D., and Yun, S. (2021a). Semiconductor electrochemistry for clean energy conversion and storage. *Electrochemical Energy Reviews* *4*, 757-792. 10.1007/s41918-021-00112-8.

Zhu, B., Mi, Y., Xia, C., Wang, B., Kim, J.-S., Lund, P., and Li, T. (2021b). Nano-scale view into solid oxide fuel cell and semiconductor membrane fuel cell: material and technology *Energy Materials*. 10.20517/energymater.2021.03.

Zhu, T., Troiani, H.E., Mogni, L.V., Han, M., and Barnett, S.A. (2018). Ni-substituted Sr(Ti,Fe)O₃ SOFC anodes: Achieving high performance via metal alloy nanoparticle exsolution. *Joule* *2*, 478-496. 10.1016/j.joule.2018.02.006.

Figure and table List

Fig. 1. Illustration of the synthesis of M@CNTs.

Fig. 2. Morphological characterizations of NiFe@CNTs. (a) SEM image of NiFe@CNTs. (b) TEM image of NiFe@CNTs and the corresponding outer diameters of CNTs ($d_{\text{mean}}=14.38$ nm). (c) HRTEM image of NiFe@CNTs. (d) HRTEM image of Fe-Ni alloy. (e) HRTEM image of CNTs. (f) HAADF-STEM cross-sectional compositional profiles. (g) Elemental mapping of C, Fe and Ni in HAADF-STEM images.

Fig. 3. Physicochemical characterization of M@CNTs. (a) N₂ adsorption-desorption isotherms and pore-size distribution curves by the N₂-DFT method of all samples. (b) XRD patterns of all samples. (c) TG curves and DTG curves of all samples. (d) High-resolution XPS spectra of Ni 2p for Ni@CNTs and NiFe@CNTs. (e) High-resolution Fe 2p XPS spectra for Fe@CNTs and NiFe@CNTs. (f) Raman spectra of all samples.

Fig. 4. Electrochemical performance and conductivity. (a) Schematic diagram of LT-SOFCs. (b) IV-IP curve for fuel cells with the cell structure. (c) Fitted equivalent circuits of EIS. (d) Comparisons with other reported works for the performances of SOFCs. (1. (Chen et al., 2018); 2. (Mumtaz et al., 2019); 3. (Mumtaz et al., 2019); 4. (Khan et al., 2020); 5.(Ahsan et al., 2020); 6. (Ajmal Khan et al., 2018); 7. (Hussain et al., 2019); 8. (Batoool et al., 2019); 9. (Zhu et al., 2018); 10. (Cao et al., 2015); 11. (Sun et al., 2016).)

Fig. 5. Density functional theory results. Calculated hydrogen adsorption energies on the

714 different sites of (a) Ni@CNTs, (b) Fe@CNTs, (c) NiFe@CNTs, (d) free energy diagrams
715 of the elementary processes of HOR on the different M@CNTs and (e) UPS spectra of
716 Ni@CNTs, Fe@CNTs and NiFe@CNTs.

Highlights

- The M@CNTs from the waste plastics were utilized as anode additive of LT-SOFCs.
- The effects of active metal species on the quality of nanocomposite were studied.
- Maximum power density of 885 mW cm^{-2} at $500 \text{ }^{\circ}\text{C}$ was obtained with NiFe@CNTs.
- The excellent performances of SOFCs could be attributed to the improved HOR activity.

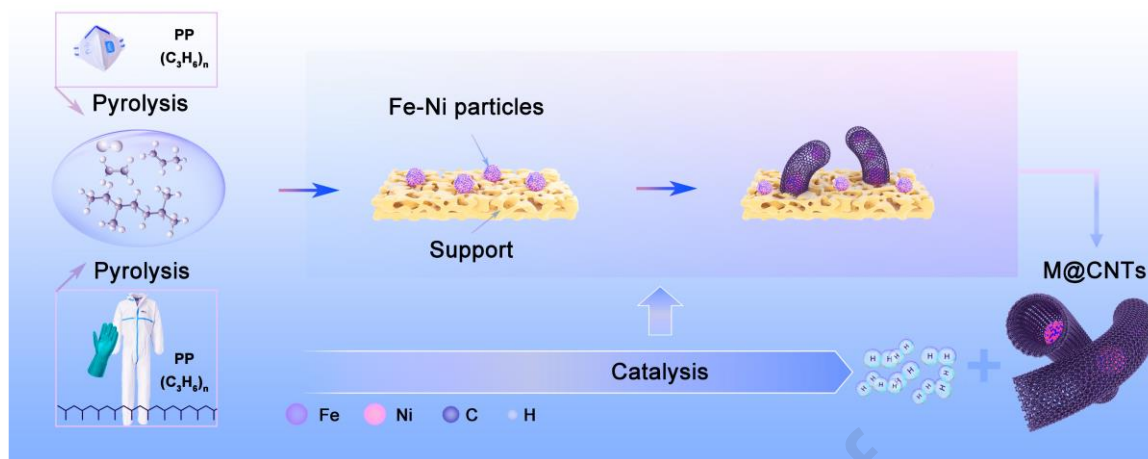


Fig. 1 Illustration of the synthesis of M@CNTs.

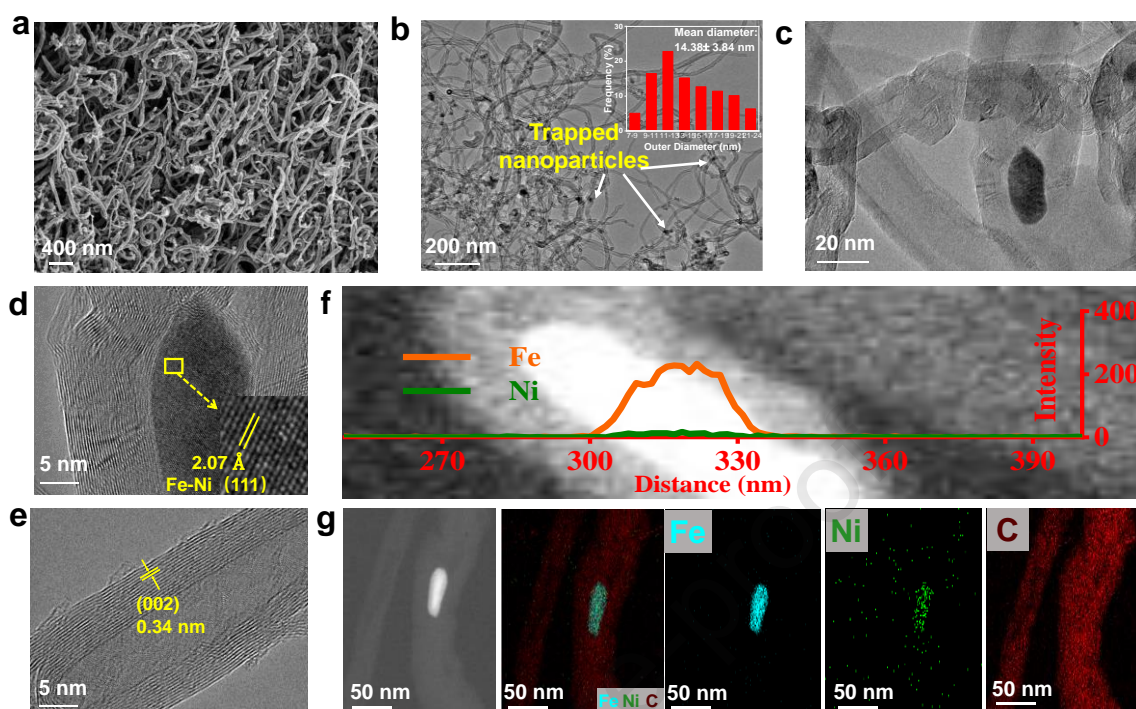


Fig. 2 Morphological characterizations of NiFe@CNTs. (a) SEM image of NiFe@CNTs. (b) TEM image of NiFe@CNTs and the corresponding outer diameters of CNTs ($d_{\text{mean}}=14.38$ nm). (c) HRTEM image of NiFe@CNTs. (d) HRTEM image of Fe-Ni alloy. (e) HRTEM image of CNTs. (f) HAADF-STEM cross-sectional compositional profiles. (g) Elemental mapping of C, Fe and Ni in HAADF-STEM images.

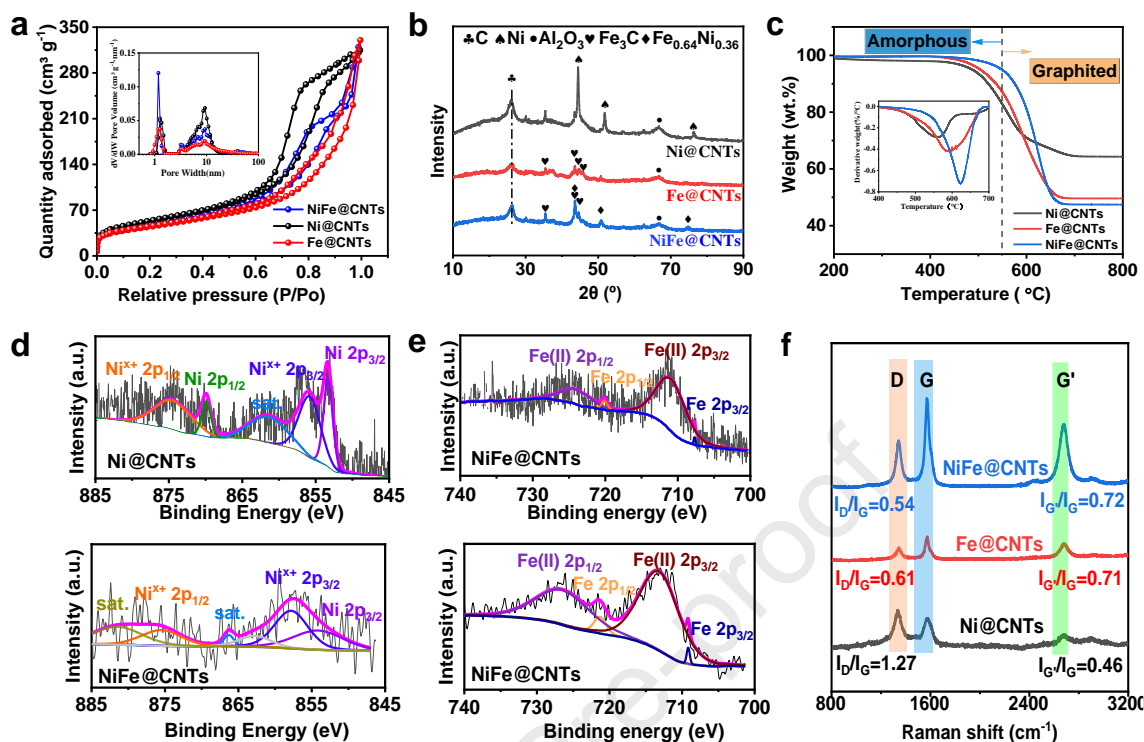


Fig. 3 Physicochemical characterization of M@CNTs. (a) N₂ adsorption-desorption isotherms and pore-size distribution curves by the N₂-DFT method of all samples. (b) XRD patterns of all samples. (c) TG curves and DTG curves of all samples. (d) High-resolution XPS spectra of Ni 2p for Ni@CNTs and NiFe@CNTs. (e) High-resolution Fe 2p XPS spectra for Fe@CNTs and NiFe@CNTs. (f) Raman spectra of all samples.

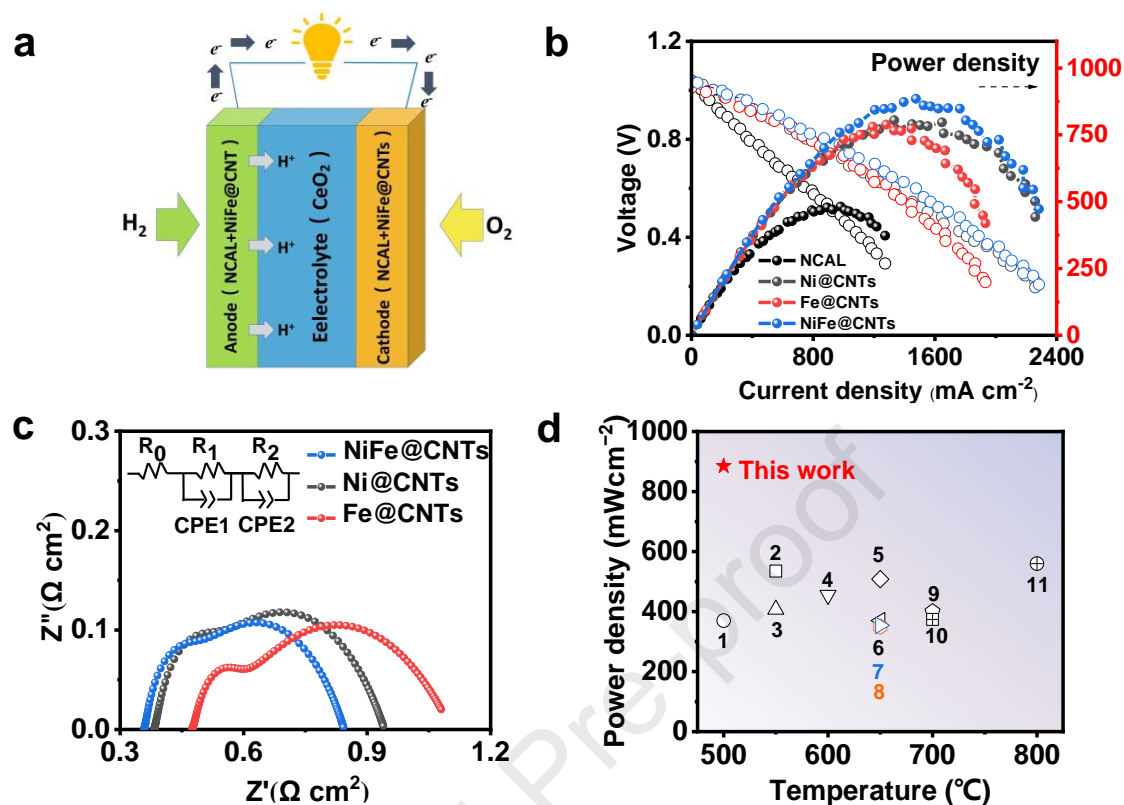


Fig. 4 Electrochemical performance and conductivity. (a) Schematic diagram of LT-SOFCs. **(b)** IV-IP curve for fuel cells with the cell structure. **(c)** Fitted equivalent circuits of EIS. **(d)** Comparisons with other reported works for the performances of SOFCs. (1. Chen et al., 2018; 2. Mumtaz et al., 2019; 3. Mumtaz et al., 2019; 4. Khan et al., 2020; 5. Ahsan et al., 2020; 6. Ajmal Khan et al., 2018; 7. Hussain et al., 2019; 8. Batool et al., 2019; 9. Zhu et al., 2018; 10. Cao et al., 2015; 11. Sun et al., 2016.)

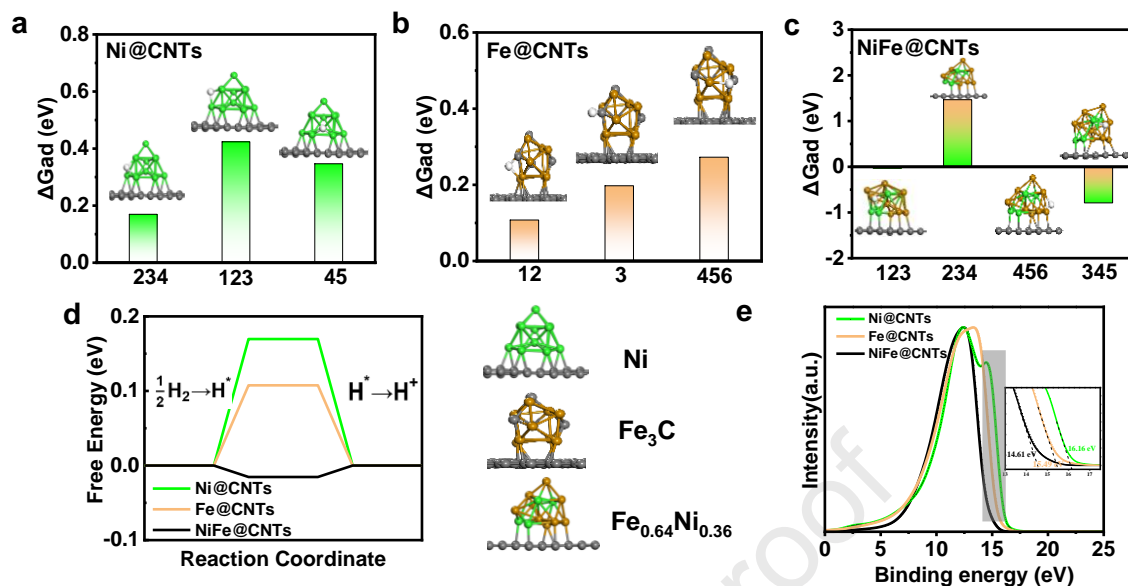


Fig. 5 Density functional theory results. Calculated hydrogen adsorption energies on the different sites of **(a)** Ni@CNTs, **(b)** Fe@CNTs, **(c)** NiFe@CNTs, **(d)** free energy diagrams of the elementary processes of HOR on the different M@CNTs and **(e)** UPS spectra of Ni@CNTs, Fe@CNTs and NiFe@CNTs.

TABLE FOR AUTHOR TO COMPLETE

Please upload the completed table as a separate document. **Please do not add subheadings to the key resources table.** If you wish to make an entry that does not fall into one of the subheadings below, please contact your handling editor. **Any subheadings not relevant to your study can be skipped.** (NOTE: For authors publishing in Cell Genomics, Cell Reports Medicine, Current Biology, and Med, please note that references within the KRT should be in numbered style rather than Harvard.)

Key resources table

REAGENT or RESOURCE	SOURCE	IDENTIFIER
Antibodies		
Bacterial and virus strains		
Biological samples		
Chemicals, peptides, and recombinant proteins		
Aluminum sec-butoxide	Aladdin	A106801; CAS:2269-22-9
Nickel nitrate hexahydrate	Aladdin	N108891; CAS:13478-00-7
Iron (III) nitrate nonahydrate	Sinopharm Chemical Reagent Co. Ltd.	80072718; CAS: 7782-61-8
Critical commercial assays		
Deposited data		
Experimental models: Cell lines		

Experimental models: Organisms/strains		
Oligonucleotides		
Recombinant DNA		
Software and algorithms		
Vienna Ab initio Simulation Package	Nie et al., 2018	https://www.vasp.at/
Other		